

Chimera States and Seizures in a Mouse Neuronal Model

Henry M. Mitchell,^{1, 2, 3, 4} Peter Sheridan Dodds,^{1, 3, 4, 5} J. Matthew Mahoney,^{5, 6} and Christopher M. Danforth^{1, 3, 4, 5}

¹⁾Department of Mathematics and Statistics, University of Vermont, Burlington, VT 05401

²⁾Department of Physics, University of Vermont, Burlington, VT 05401

³⁾Vermont Complex Systems Center, University of Vermont, Burlington, VT 05401

⁴⁾Computational Story Lab, University of Vermont, Burlington, VT 05401

⁵⁾Department of Computer Science, University of Vermont, Burlington, VT 05401

⁶⁾Department of Neurology, University of Vermont Larner College of Medicine, Burlington, VT 05401

Chimera states—the coexistence of synchrony and asynchrony in a nonlocally-coupled network of identical oscillators—are often used as a model framework for epileptic seizures. The present study explores the dynamics of chimera states in a network of modified Hindmarsh-Rose neurons, configured to reflect the graph of the mesoscale mouse connectome. Our model produced superficially epileptiform activity converging on persistent chimera states in a large region of a two-parameter space governing connections (a) between subcortices within a cortex and (b) between cortices. The findings contribute to a growing body of literature suggesting mathematical models can qualitatively reproduce epileptic seizure dynamics.

I. INTRODUCTION

A. Chimera States

The science and mathematics of synchronization are among history's most well-studied areas of research. One of the earliest well-documented appearances of synchrony in unexpected places was observed in 1665 by Dutch physicist Christiaan Huygens, the inventor of the pendulum clock. He noticed that two clocks hung from the same beam would eventually synchronize with each other. He supposed that this was due to minuscule energy transfers between the two clocks through the wooden beam. This hypothesis was proven nearly 350 years later which shows that even the simplest-seeming synchronization behavior results from complex dynamics¹.

This behavior extends to larger systems than two clocks. A classic demonstration in many classes on the mathematics of synchronization depicts the same phenomenon with more oscillators². One places a platform on top of a set of rollers, and places at least two metronomes on that platform (see Fig. 1 for a drawing). When these metronomes are started with the same frequency, out of phase with each other, over time their phases drift until they synchronize.

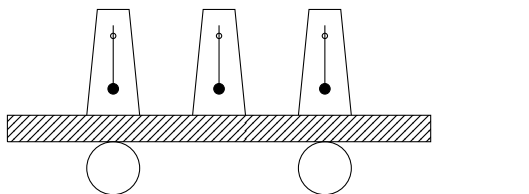


FIG. 1. The classic demonstration of Huygens synchronization. When the metronomes are set running, they eventually synchronize due to the light coupling provided by the platform's ability to roll.

One example of more complex behavior arising from

similar mechanisms is the coexistence of synchrony and asynchrony within a system of identical coupled oscillators, a phenomenon known as a *chimera state*^{3,4}. The existence of these chimera states are surprising, as they represent asymmetry within symmetric systems. The first time this behavior was observed was in a ring of *nonlocally coupled* oscillators³. While global coupling is an all-to-all interaction and local coupling is a nearest-neighbor interaction, nonlocal coupling is a mixture of the two. The model is expressible in one dimension as

$$\frac{\partial}{\partial t}A(x,t) = (1 + i\omega_0)A - (1 + ib)|A|^2A + K(1 + ia)(Z(x,t) - A(x,t)) \quad (1)$$

where

$$Z(x,t) = \int G(x - x')A(x',t) dx'$$

and

$$G(y) = \frac{\kappa}{2}e^{-k|y|},$$

which reduces to the phase equation

$$\frac{\partial}{\partial t}\phi(x,t) = \omega - \int G(x - x') \times \sin(\phi(x,t) - \phi(x',t) + \alpha) dx' \quad (2)$$

where

$$\tan(\alpha) = \frac{b - a}{1 + ab}. \quad (3)$$

We numerically simulated the Kuramoto system using a discrete approximation, and it quickly fell into a chimera state (Fig. 2).

Since then, chimera states have been found in simpler systems still. One of the simplest is the Abrams model, two populations of identical oscillators with a stronger

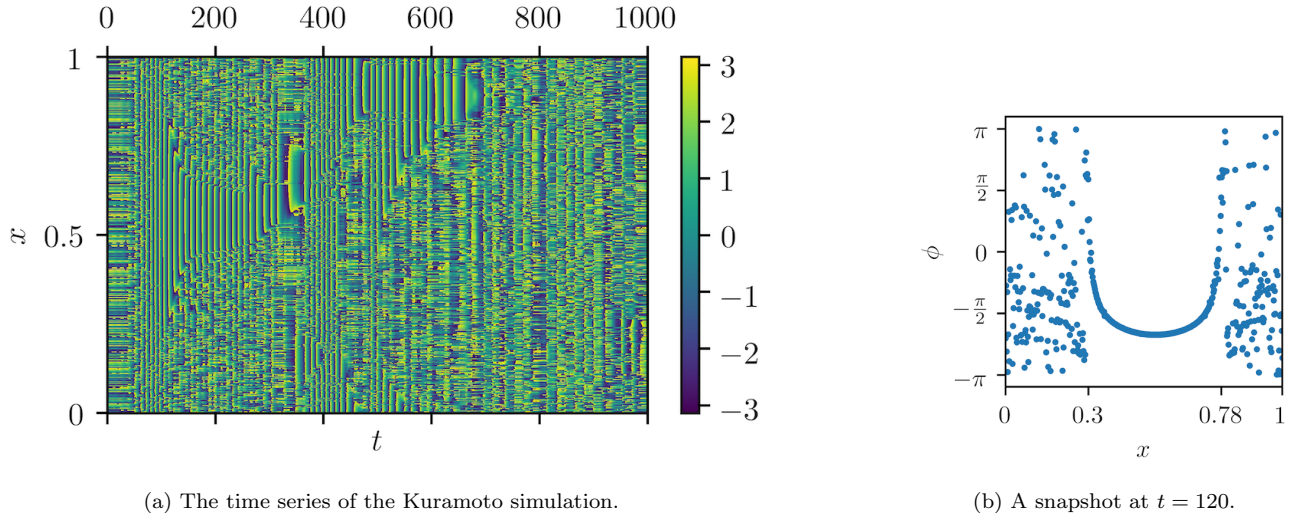


FIG. 2. The results of our simulation of a Kuramoto oscillator, as described in Eq. (2). A 4th-order Runge-Kutta solver ($dt = 0.01$, $t_{\max} = 1000$) was run on a system of 512 oscillators. (a) The entire time series of the simulation. The behavior represented there is quite complex, with several distinct qualitative changes to the patterns in the system. However, in-depth analysis of this system is beyond the purview of this work. (b) A snapshot of the state of the system at $t = 120$. Note the juxtaposition of asynchronous ($0 \lesssim x \lesssim 0.3$ and $0.78 \lesssim x \lesssim 1$) and synchronous (oscillators $0.3 \lesssim x \lesssim 0.78$).

coupling strength within the populations than between them⁵. The equation describing this system is given as

$$\frac{d\theta_i^\sigma}{dt} = \omega + \sum_{\sigma'=1}^2 \frac{K_{\sigma\sigma'}}{N_{\sigma'}} \sum_{j=1}^{N_{\sigma'}} \sin(\theta_j^{\sigma'} - \theta_i^\sigma - \alpha) \quad (4)$$

where

$$K = \begin{bmatrix} \mu & \nu \\ \nu & \mu \end{bmatrix} \quad \text{and} \quad \sigma \in \{1, 2\}.$$

In this model, μ represents the intra-population strength, and ν represents the inter-population strength, meaning $\mu > \nu$. Time can be scaled such that $\mu + \nu = 1$. If $\mu - \nu$ is not too large, and α is not too much less than $\frac{\pi}{2}$, then this system can produce chimera states. Fig. 3 shows a simulation of the Abrams model on two populations of 128 oscillators.

A similar system was also analyzed in the physical world⁶. Two swinging platforms were coupled together with springs of variable spring constant κ , and 15 metronomes—all tuned to the same frequency—were placed on each platform. For a wide range of values of κ , all of the metronomes on one platform would synchronize, while the metronomes on other platform would remain asynchronous. This system is directly analogous to the Abrams model. The metronomes on the same platform are coupled through the motion of the swing, which heavily influences the motion of the metronomes. This intra-population coupling is represented by μ in the Abrams model. The metronomes on opposite platforms are coupled through the springs, which is a much weaker interaction, represented in the Abrams model by ν .

While chimera states may present themselves obviously when observed in a plot or the physical world,

they can be harder to pin down analytically. One useful pair of measures for the presence of a chimera state are the *chimera-like index* χ and the *metastability index* m ^{7,8}. We will investigate a system of M communities of nonlocally-coupled oscillators, and we sample their phases at times $t \in [1, \dots, T]$. In order to develop these two measures, one must first develop the *order parameter* $r(t) = |\langle e^{i\phi_k(t)} \rangle_{k \in C}|$, where ϕ_k is the phase of oscillator k , and $\langle f \rangle_{k \in C}$ is the average of f over all k in community C . r indicates the instantaneous synchrony of a community (how similar the phases of the oscillators are to the others in C), and not its overall coherence (how similar the trajectories of the oscillators are). From this, we find the two measures:

$$\chi = \langle \sigma_{\text{chi}} \rangle_T \quad (5)$$

$$m = \langle \sigma_{\text{met}} \rangle_C \quad (6)$$

where

$$\sigma_{\text{chi}}(t) = \frac{1}{M-1} \sum_{c \in C} (r_c(t) - \langle r_c \rangle_C)^2 \quad (7)$$

$$\sigma_{\text{met}}(c) = \frac{1}{T-1} \sum_{t \leq T} (r_c(t) - \langle r_c \rangle_T)^2 \quad (8)$$

To put this into words, the metastability index is the average across communities of the variance of the order parameter within a given community over time, while the chimera-like index is the average over time of the variance of the order parameter across communities.

This gives us some maximum possible values for these measures⁷. If a community c spends equal time in all stages of synchronization (i.e., the phase parameter of c is uniformly distributed), then $\sigma_{\text{met}}(c)$ is at

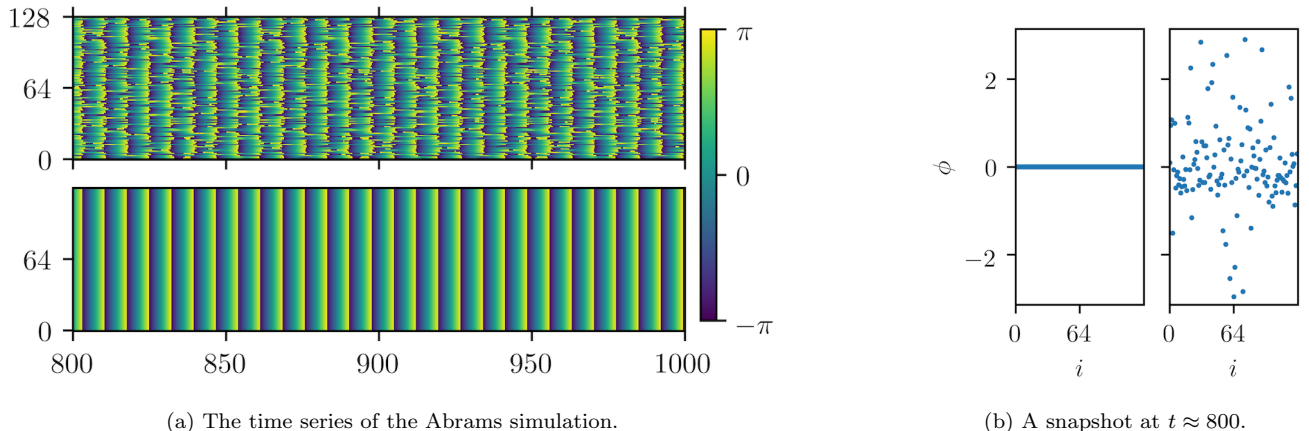


FIG. 3. A simulation of the Abrams model for two populations of 128 oscillators. A 4th-order Runge-Kutta solver ($dt = 0.01$, $t_{\max} = 1000$) was run. (a) shows the time series of the simulation for $t \in (800, 1000)$. (b) shows a snapshot at $t \approx 800$.

its maximum, the variance of the uniform distribution: $m_{\max} = \frac{1}{12}$. If a community spends equal time in a maximally chimeric state and a minimally chimeric state, then its chimera-like index will be at its maximum¹: $\chi_{\max} = \frac{1}{7}$. Therefore, when the normalized chimera-like and metastability indices are presented, they will be presented normalized to $\frac{1}{7}$ and $\frac{1}{12}$, respectively.

Chimera states have been observed in many other systems, whether they be purely mathematical, biological, electrical, or mechanical^{3,4,6–14}. One of the most common ways that chimera states are talked about is in regards to seizures.

B. Seizures

1. Neuroanatomy and Neurophysiology

Since the brain is an electrochemical device, its function and disorders are often best talked about from an electrical standpoint¹⁵. *Neurons* are cells which are specialized for communication (see Fig. 4 for a diagram). They receive input signals through *synapses* at the ends

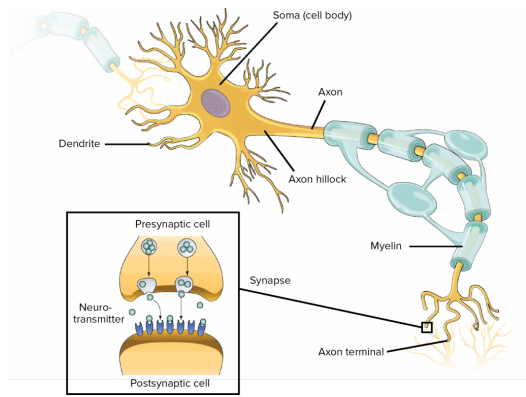


FIG. 4. A diagram of the anatomy of a neuron. Taken from¹⁶.

of their *dendrites*, branches in their large tree of inputs. The trunk of the dendritic tree is the *soma*, the cell body. If the sum signal entering the soma from all of the dendrites is sufficient, the neuron *fires*, sending a signal to its outputs.

When a neuron fires, it sends an electrochemical signal down its *axon*—its long stem—to the output synapses at its *axon terminals*. This signal is known as an *action potential*. The action potential is discrete; a neuron sends the same signal any time its input threshold is surpassed, no matter how far above the threshold the input is. It is the propagation along the axon of a potential difference across the cell membrane of the neuron. This potential difference is created by different concentrations of various ions in and out of the cell, controlled by pumps (which push Na^+ out of the cell and draw K^+ into it) and gates (which allow the ion concentrations to equilibrate). It is important to note that processes involving Na^+ are faster than those involving K^+ . Each location along the axon goes through the following six stages, in total taking approximately 1 ms:

Equilibrium: No current flows through the membrane,

¹ While it is possible for half of a system's communities to be synchronous and the other half asynchronous for all times (resulting in a chimera-like index of $\frac{2}{7}$), this is transient due to the effects of metastability⁷. Therefore, we will ignore this case.

which has a potential of -75 mV across it².

Depolarization: The potential difference propagating from upstream in the axon activates ion channel gates, allowing Na^+ to flow into the axon, countered by the K^+ flowing out.

Amplification: Because the K^+ processes are slower than the Na^+ processes, if the incoming signal is strong enough, the influx of Na^+ is too fast for the outflow of K^+ to compensate. This results in a positive feedback loop, wherein the Na^+ flowing in increases the membrane potential, which increases the rate at which Na^+ flows into the neuron, which continues to feed itself.

Repolarization: When the Na^+ channels are fully open, the K^+ channels are finally able to compensate for the influx.

Hyper-polarization: The Na^+ channels close, and the slower K^+ channels remain open. This causes more K^+ to flow out of the cell than Na^+ flowed in, dropping the potential below its equilibrium state.

Refractory Period: The Na^+ channels are briefly unable to open, which means that neurons need a brief time to “recharge” after an action potential.

All of these processes are summarized in the *Hodgkin-Huxley model*³ describing the membrane potential U :

$$C_m \dot{U} + p_{\text{AK}^+} \bar{g}_{\text{AK}^+} (U - E_{\text{K}^+}) + p_{\text{A}\text{Na}^+} \bar{g}_{\text{A}\text{Na}^+} (U - E_{\text{Na}^+}) + g_l (U - E_l) = I_m \quad (9)$$

where

$$\begin{aligned} \dot{n} &= \alpha_n(1-n)\beta_n n \\ \dot{m} &= \alpha_m(1-m)\beta_m m \quad \text{and} \quad p_{\text{AK}^+} = n^4 \\ \dot{h} &= \alpha_h(1-h)\beta_h h \quad p_{\text{A}\text{Na}^+} = m^3 h \end{aligned} \quad (10)$$

where g_i is the conductance of the membrane to ion i , p_{Ai} is the proportion of i -gates which are open (developed from a Markov model with transition rates α and β), E_i is the equilibrium potential of ion i , C_m is the capacitance of the membrane, and I_m is an external current (the tuned input parameter). This model is highly accurate, and won its developers a Nobel Prize in Physiology or Medicine. Many bifurcation analyses have been performed on these equations, and they are well understood¹⁷.

However, the Hodgkin-Huxley model is not particularly useful for large-scale brain simulation. Given that most behavior of the brain is emergent⁴, it is important

to understand neurons' interactions. As is often the case with emergent phenomena, it is wildly impractical to simulate the collective behavior of a brain by simulating its constituent neurons. Since the human brain has approximately 10^{11} neurons with 10^{14} synapses, direct simulation is too computationally intensive. In order to better understand the dynamics of large portions of the brain, many researchers turned to the techniques of thermal and statistical physics¹⁸. Particularly, *neural ensemble models* and *neural mass models* are popular approaches to studying brain behavior.

Neural ensemble models treat patches of the brain as a collective group, taking into account neurons' mean activity, as well as their variance. They assume that the firings of the neurons within a group are sufficiently uncorrelated to result in a Gaussian distribution of firing rates. This means that the behavior of the ensemble is linear, even though the behavior of the constituent neurons is highly nonlinear. One can then use a Fokker-Planck equation to describe the collective dynamics of the population. The main benefit to these models is that they are well-studied in fields like solid-state physics. However, recent work has shown that the assumption of Gaussian firing rates is not accurate¹⁸. Firing rates do tend to fall into well-behaved distributions, but not ones that lend themselves to already-developed tools.

For higher coherence within populations (i.e., a non-Gaussian distribution of firing rates), researchers tend to use neural mass models. They assume that nearby neurons in the brain are sufficiently synchronized to model groups of them as a single neuron, with some modifications. Instead of the discrete action potential of a single neuron, neural mass models often have a sigmoidal activation function. They will also simplify the dynamics of the Hodgkin-Huxley model to divide the neural mass's constituent neurons into two subpopulations: an excitatory pool (corresponding to the Na^+ channels in the Hodgkin-Huxley model) and an inhibitory pool (corresponding to the K^+ channels in the Hodgkin-Huxley model).

An example of a neural mass model is the extremely simple Wilson-Cowan model¹⁹:

$$\tau_x \dot{x} = -x + S(C_{xx}x + C_{xy}y + C_{xz}z + P) \quad (11)$$

$$\tau_y \dot{y} = -y + S(C_{yx}x + C_{yy}y + C_{yz}z + Q) \quad (12)$$

$$\tau_z \dot{z} = -z + S(C_{zx}x + C_{zy}y + C_{zz}z + R) \quad (13)$$

x represents an excitatory process (like the flow of Na^+), and y and z represent inhibitory processes (like the flow of K^+). The time constants τ_i determine the rates of the dynamics of the three processes. It is worth noting that chaotic dynamics can occur when multiple different time scales are present¹⁸. The coupling strengths C_{ij} represent the connectivity between the three processes, with $C_{ix} \geq 0$ (making x excitatory) and $C_{i\{y,z\}} \leq 0$ (making y inhibitory). P , Q , and R represent the excitability threshold, or the constant external inputs to each process (similar to I_m in Eq. (9)). The sigmoidal activation function $S(x) = \frac{1}{1+e^{-a(x-\theta)}}$ represents the mass effect of

² All potentials hold the extracellular matrix at 0 V. In other words, the interior of the cell is at a lower potential than the exterior.

³ A full derivation of this model can be found in¹⁷.

⁴ One of the classic ways to explain emergence is asking, “Where is the thought in a neuron?”

the population of neurons being modeled. This system provides an excellent toy model which reflects meso-scale dynamics accurately, relative to its simplicity.

These models do an accurate job of representing the behavior of small parts of the brain. However, it is not reasonable to carry the assumptions of un- or highly-correlated activity to the large-scale activity of whole-brain dynamics. In order to make these models accurately depict the overall behavior of the brain as a whole, researchers turn to two main techniques: *neural field models* and *neural mass networks*. The first treats the brain as a continuous sheet of cortex, within which activity obeys wave equations. The second represents the brain as a discrete graph of cortices, or a network of coupled oscillators. The graph used for the coupling of the oscillators is determined by the brain's connectivity matrix, or *connectome*. An example of a neural mass network model is the modified Hindmarsh-Rose model (Eqs. (23) to (25)), which is discussed later.

One of the benefits of a neural mass network model is that its outputs are similar to those of an *electroencephalograph*, or *EEG*. The EEG is a device used to record the electrical activity of the brain. Electrodes are placed in specific areas on the scalp, and then measure changes in voltage from neural masses beneath the skull. Much of the signal is distorted and attenuated by the bone and tissue between the brain and the electrodes, which act like resistors and capacitors. This means that, while the membrane voltage of the neuron changes by millivolts, the EEG reads a signal in the microvolt scale²⁰. Additionally, the EEG has relatively low spatial and temporal resolution (16 electrodes for the whole brain, and a sampling rate of 33 ms). However, when properly treated, neural mass models make for effective predictors of the output from EEGs^{21,22}. This is useful, as EEGs are the main tool used to detect and categorize seizures.

2. Seizure Aetiology

For centuries, and across many cultures, seizures were viewed as holy and mystical events, and those with epilepsy were often considered to be shamans^{20,23}. Seizures are often accompanied by strange visions, sounds, or smells (called *auras*), and sometimes manifest themselves physically in extreme ways. External symptoms can include convulsions of the limbs or the entire body, or a seeming trance. In societies that are unfamiliar with the root causes of seizures, this can be a terrifying and awe-inspiring sight to behold.

In more recent years, researchers have come to define seizures as abnormal, excessive, or overly-synchronized neural activity^{20,24}. It is important to distinguish between seizures and epilepsy, as the two are often conflated. Seizures are an acute event, whereas epilepsy is a chronic condition of repeated seizures. While classification schemes vary, all center around the division between *generalized* and *focal* seizures.

Generalized seizures involve the entire brain, and start in both hemispheres at the same time, which is why they are often called *primary generalized seizures*. The manifestation of these seizures crosses an entire spectrum. They sometimes hardly present to an external observer, as in the case of the *typical absence seizure*⁵, which is nonconvulsive and results in a complete cessation of motor activity for approximately 10 seconds. Patients lose consciousness, but not posture, making it seem to an observer like a trance or simply “spacing out.”

On the other side of the range is the *tonic-clonic seizure*, wherein effectively all of a patient's muscles contract at once for around 30 seconds (the tonic phase), and then clench and unclench rapidly, resulting in jerking of the extremities (the clonic phase) for 1 to 2 minutes. After tonic-clonic seizures (in the *postictal* phase), patients often report confusion, muscle soreness, and exhaustion.

Focal seizures start in one part of the brain (the seizure *focus*). They are generally preceded by auras such as a sense of fear, or hearing music, and often manifest as clonic movement of the extremities. In many cases, they secondarily generalize, spreading to the entire brain. This can make focal seizures and primary generalized seizures hard to distinguish, as a focal seizure can generalize rapidly after a brief aura. This can lead to misdiagnoses and improper treatments.

From careful observation, an empirical/phenomenological seizure model called Epileptor was developed^{25,26}. It involves two fast processes x_1 and y_1 , two *spike-wave event* processes x_2 and y_2 , and a slow permittivity variable z . Its guiding equations are:

$$\dot{x}_1 = y_1 - f_1(x_1, x_2) - z + I_{\text{rest}1} \quad (14)$$

$$\dot{y}_1 = y_0 - 5x_1^2 - y_1 \quad (15)$$

$$\dot{z} = \frac{1}{\tau_0}(4(x_1 - x_0) - z) \quad (16)$$

$$\begin{aligned} \dot{x}_2 = & -y_2 + x_2 - x_2^3 + I_{\text{rest}2} \\ & + 0.002g(x_1) - 0.3(z - 3.5) \end{aligned} \quad (17)$$

$$\dot{y}_2 = \frac{1}{\tau_2}(-y_2 + f_2(x_1, x_2)) \quad (18)$$

where

$$g(x_1) = \int_{t_0}^t e^{-\gamma(t-\tau)} x_1(\tau) d\tau \quad (19)$$

$$f_1(x_1, x_2) = \begin{cases} x_1^3 - 3x_1^2, & \text{if } x_1 < 0 \\ x_1(x_2 - 0.6(z - 4)^2), & \text{if } x_1 \geq 0 \end{cases} \quad (20)$$

$$f_2(x_1, x_2) = \begin{cases} 0, & \text{if } x_2 < -0.25 \\ 6(x_2 + 0.25), & \text{if } x_2 \geq -0.25 \end{cases} \quad (21)$$

The required parameters have the following values: $x_0 = -1.6$, $y_0 = 1$, $\tau_0 = 2857$, $\tau_1 = 1$, $\tau_2 = 10$, $I_{\text{rest}1} =$

⁵ Since a lot of early epilepsy research was performed in French-speaking regions, “absence” is pronounced æb’sans.

3.1 , $I_{\text{rest}2} = 0.45$, $\gamma = 0.01$. A feature to note is that $\tau_0 \gg \tau_2 \gg \tau_1$. As previously mentioned, these vastly different time scales allow for chaotic dynamics to occur, and contribute to the nonlinearity of the system.

While the Epileptor model is highly accurate, and is currently being used to develop patient-specific models and treatments, its main issue is that it is purely phenomenological. EEG traces of humans, mice, and zebrafish were collected, and parameters were adjusted until $x_1 + x_2$ matched the measured traces, resulting in the above values. This means that, while the variables and parameters in the model directly correspond to physical processes, the model's development was largely empirical, and not fully rooted in theory²⁵. This means that it can be a helpful tool in treating symptoms, but is not necessarily as valuable for determining root causes.

II. LITERATURE REVIEW

It is important to get a sense of how the area of nonlinear dynamics has been applied to neuroscience. One of the most powerful tools for describing the qualitative behavior of a nonlinear system is *bifurcation analysis*, determining how the number and stability of fixed points and limit cycles changes as parameters of a model change²⁷.

A. Bifurcation Analyses of Seizure Models

Analyses of the dynamics of brain models can provide an understanding of the mechanisms underlying a wide variety of brain behaviors. Multistability and bifurcations can be interpreted as being at the center of many different states, from seizures to switching from syncopated to anti-syncopated finger tapping^{12,18,19,24,25,28}. With that in mind, it is worthwhile to look at some examples of bifurcation analyses of neural models.

1. The Wilson-Cowan Model

One of the simplest models which lends itself to bifurcation analysis is the Wilson-Cowan model (Eqs. (11) to (13)). Traces of x over time look remarkably like the output from an EEG scan. Fig. 5 shows a simulation of the Wilson-Cowan model with the parameters⁶:

$$C = \begin{bmatrix} 23 & -15 & -10 \\ 35 & 0 & 0 \\ 10 & 0 & 0 \end{bmatrix}, \quad \begin{bmatrix} P \\ Q \\ R \end{bmatrix} = \begin{bmatrix} 3 \\ -5 \\ -5 \end{bmatrix}, \quad (22)$$

$$\tau = \begin{bmatrix} 0.015 \\ 0.013 \\ 0.267 \end{bmatrix}$$

These results show a stereotypical spike-wave event, represented to a high degree of accuracy relative to the simplicity of the model.

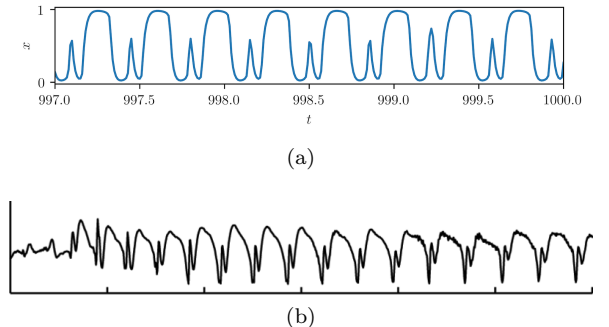


FIG. 5. A comparison of a simulation of the Wilson-Cowan system and an actual EEG trace of spike-wave event. (a) The output of a simulation of the Wilson-Cowan model (Eqs. (11) to (13)) using parameters from¹⁹. A 4th-order Runge-Kutta solver ($dt = 0.01$, $t_{\text{max}} = 1000$) was run on the Wilson-Cowan model with parameters shown in Eq. (22). (b) An EEG trace of a spike-wave event, often characteristic of absence seizures. Taken and modified from²⁹.

The main challenge to performing bifurcation analysis on this type of system is two-fold. The first aspect is that there are 15 parameters to vary. This makes bifurcation analysis exceedingly difficult, as all 15 dimensions and their relationships to each other must be analyzed. This is closely related to the second aspect of the challenge this model provides: the variables in this model are abstracted from their physical/physiological meanings. For example, because the coupling strengths do not correspond directly to any measurable values, it is hard to gain actionable semantic knowledge from analysis of their effects on the system²⁵.

However, it is possible to observe a bifurcation if the external input P varies (Eq. (11)). Fig. 6 shows the change from spike-wave behavior to simple wave behavior as P increases past 3.92, at time 47.3. While it would be impossible to do an exhaustive sweep of parameter space, one can observe all of the dynamics of brain behavior in this model.

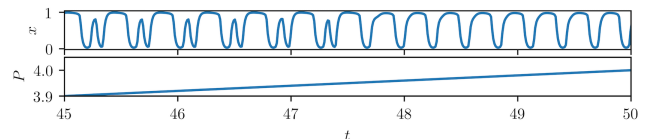


FIG. 6. A bifurcation from spike-wave behavior to simple wave behavior in the Wilson-Cowan model as a function of continuously varying external input parameter P . Simulation used a 4th-order Runge-Kutta solver ($dt = 0.01$, $t_{\text{max}} = 100$) as P linearly increased from 3 to 5.

⁶ Parameters taken from¹⁹, table 1. Note that the values in rows 3(g), 3(i) and 3(j), 3(l) should be switched.

2. The Epileptor Model

In the Epileptor model (Eqs. (14) to (21)), bifurcations depending on the slow permittivity variable z determine whether the brain is behaving normally, or having a seizure²⁵. Given the time scale on which z varies ($\frac{1}{2857}$ times as fast as x_1) and the bifurcations' dependence on it, it acts like an external parameter to the system, causing the model to go into and out of seizure. In Fig. 7, the transitions into and out of seizure are clear as critical points in z . Particularly, as is the case with many similar models, normal steady-state brain function corresponds to a stable fixed point, while seizure-like events are on stable limit cycles. This raises the question: what kinds of bifurcations occur during the transition from healthy brain activity to seizures and back?

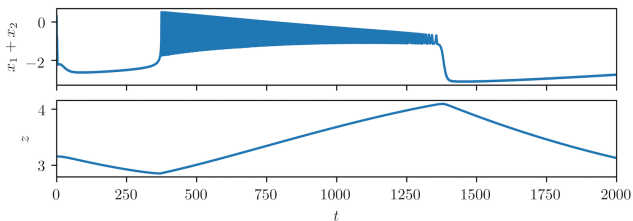


FIG. 7. A simulation of the Epileptor model showing the observable x_1 and the slow-changing permittivity variable z , using a 4th-order Runge-Kutta solver ($dt = 0.01$, $t_{\max} = 2000$) and the parameters listed in Section IB 2. The brain is exhibiting healthy behavior for $t \in (0, 360) = h_1$, then rapidly jumps into a seizure-like behavior. It stays in this state for $t \in (360, 1360) = s$, until it returns to a healthy fixed point for $t \in (1360, 2000) = h_2$. Note the DC shift, wherein $x_1(s) > x_1(h_1) \approx x_1(h_2)$.

To discuss the dynamics of Epileptor in general, we will use the stereotypical behavior displayed in Fig. 7. An important aspect of epileptor to note is that $x_1 + x_2$ is the closest variable to an observable quantity, but it still does not resemble an EEG trace without some post-processing. Particularly, x_1 would look a lot more like the output from an EEG if put through a high-pass filter. However, there is an invertible map directly between $x_1 + x_2$ and the readings from an EEG, so the results can be treated as the same²⁵.

During seizure onset at $t = 360$, the stable fixed point of healthy activity disappears, replaced by a stable limit cycle. This indicates that the system undergoes either a Hopf or a saddle-node bifurcation. A hint towards the type of bifurcation involved is that seizures occur suddenly²⁰. This means that the amplitude of oscillation does not steadily increase from 0, meaning that a supercritical Hopf bifurcation can be ruled out²⁷. At $t = 360$, the mean values of $x_1 + x_2$ jump from $\langle x_1(t) + x_2(t) \rangle_{t \in h_1} = -2.5$ to $\langle x_1(t) + x_2(t) \rangle_{t \in s} = -0.8$. This DC shift does appear in experiment, and indicates that the bifurcation can not be a subcritical Hopf. This leaves only a saddle-node bifurcation for the transition into a seizure²⁵.

As the seizure ends at $t = 1360$, the model returns from a limit cycle to a fixed point with another DC shift. This indicates that the bifurcation is either a fold bifurcation or a homoclinic bifurcation. One important point of note is that the frequency of oscillation decreases as the seizure approaches offset, which matches with experiment. This indicates that the transition must be a homoclinic bifurcation, because systems maintain constant frequency as they approach fold bifurcations²⁵.

B. Chimera States in the Brain

Chimera states in brain models have often been linked loosely to unihemispheric sleep, seizures, and other brain behaviors^{4–7,10,30–32}. In most cases, these connections are made in off-hand remarks to introduce the concept of a chimera state, but serious connections between these phenomena are rarely drawn. However, there are some notable cases of investigations of chimera states in brains.

1. Square Torus

One such example is an investigation of two different neural models (FitzHugh-Nagumo neurons and leaky integrate-and-fire neurons, both known to be accurate neural models¹⁵) run on a toroidal square network of $N \times N$ nonlocally coupled neurons³³. The most important result of this simulation is that similar behaviors appeared in each. It was found that FitzHugh-Nagumo and leaky integrate-and-fire neurons not only can produce chimera states, but produce chimera states in similar shapes and patterns.

For example, both types of neurons produced isolated disks of high synchrony while the rest of the torus was oscillating asynchronously (coherent-spot), as well as disks of asynchrony while the rest of the system was oscillating synchronously (incoherent-spot). Both types of neurons also produced states in which a ring of neurons were firing synchronously between two areas of asynchronous oscillation (coherent-ring), and vice versa (incoherent-ring).

This similar behavior indicates that the presence of chimera states is not simply a function of the precise model chosen, but a quality universal to brain activity. Thus, it makes sense to postulate that chimera states will appear in any reasonably accurate brain model. The main caveat for that takeaway is that the network topology chosen for these models was not necessarily representative of the topology of an actual brain (see Section III B). However, seeing as the models both presented chimera-like behavior, these states are well worth pursuing in other models.

2. Chimera Collapse

Chimera states are transient behavior for finite networks of oscillators³⁴. This means that a finite number of oscillators will eventually collapse into a totally synchronous state. This transition occurs suddenly, but does provide warning signs. As the system gets closer to collapse, the asynchronous group gets increasingly incoherent⁹. This is counterintuitive, as the asynchronous group is already almost incoherent (by definition). However, the order parameter of an asynchronous group is rarely 0. As an example, in the snapshot of the simulation of the Kuramoto model (Fig. 2b), the asynchronous group is generally gathered around $\phi = -\frac{\pi}{2}$. The asynchronous group's non-zero coherence provides it its own mean-field (however spread it may be), which protects it from being absorbed into the synchronous group. Thus, when the coherence of the asynchronous group decreases, this mean-field goes away, leaving the asynchronous group susceptible to collapse.

This hypo-coherence preceding chimera state collapse was observed in transcranial EEG recordings of patients undergoing seizures⁹. However, the authors were very clear that the analogies between chimera state collapse and seizures are extremely conceptual. It has yet to be shown whether chimera state collapse specifically is related to seizure activity in any way.

3. Chimeras in a Cat Model

A final example of a chimera state being investigated in neural models (and the inspiration for this work) was an exploration of chimera states on a network of Hindmarsh-Rose neurons (Eqs. (23) to (25))¹². This model was simulated on the connectome of a cat (Fig. 8). Parameter space for the two connection strengths α and β was explored. Chimera states are most prevalent for low values of β , the inter-cortex connection strength¹². This is unsurprising. If the inter-cortex connection strength is too high as compared to the intra-cortex connection strength, the coupling acts global instead of nonlocal. This means that each cortex has less holding it together than pulling it apart, allowing the system to descend into asynchrony.

Additionally, with increasing input current I_0 (and increasing noise in the input current), chimera states give way to incoherence. This also intuitively makes sense. As the input current increases, its significance relative to the coupling also increases. Thus, the oscillators have no reason to synchronize. And, of course, adding noise will simply amplify the effect.

III. METHODS

The main analysis in this work is a modification of work by Santos *et al.*¹².

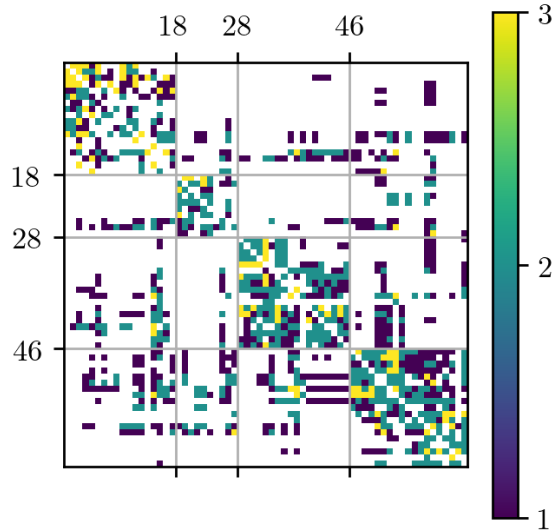


FIG. 8. The cat connectome, represented as a matrix. The cat brain was divided into 4 cortices (visual, auditory, somato-motor, and frontolimbic) with 65 subcortices. The connection strength between the subcortices was measured and placed on a scale of 1, 2, or 3.

A. Model

The model used for this work was the modified Hindmarsh-Rose neural model⁷ taken from [12].

$$\dot{x}_j = y_j - x_j^3 + bx_j^2 + I_j - z_j \quad (23)$$

$$-\frac{\alpha}{n'_j} \sum_{k=1}^N G'_{jk} \Theta_j(x_k) - \frac{\beta}{n''_j} \sum_{k=1}^N G''_{jk} \Theta_j(x_k) \quad (24)$$

$$\dot{y}_j = 1 - 5x_j^2 - y_j \quad (24)$$

$$\dot{z}_j = \mu(s(x_j - x_{\text{rest}}) - z_j) \quad (25)$$

where

$$\Theta_j(x_k) = \frac{x_j - x_{\text{rev}}}{1 + e^{-\lambda(x_k - \theta)}} \quad (26)$$

is the sigmoidal activation function. This activation function helps the model better approximate the behavior of neural masses, as opposed to specific neurons. Table I shows the values and meanings of the symbols in the model.

This model was chosen due to the semanticity of its parameters, as well as its proven ability to exhibit chimera-like behavior as a neural mass model¹². Additionally, the Hindmarsh-Rose model was not designed to emulate seizures, which provides further evidence for the theory that chimeras are a universal aspect of brain activity, as discussed in Section II B 1.

⁷ The modification is to add in the coupling, turning it into a network model instead of a single neuron.

Symbol	Value	Meaning
x_j	—	Membrane potential of the j th neural mass
y_j	—	Associated with the fast processes
z_j	—	Associated with slow processes
b	3.2	Tunes the spiking frequency
I_j	4.4	External input current
x_{rev}	2	Ambient reverse potential
λ	10	Sigmoidal activation function parameter
θ	-0.25	Sigmoidal activation function parameter
μ	0.01	Time scale for variation of z
s	4	Governs adaptation
x_{rest}	-1.6	Resting/equilibrium potential
α	Varied	Connection strength within cortices
n'_j	See Fig. 10a	Number of connections within a cortex from the j th neuron
G'_{jk}	See Fig. 10b	Intra-cortical connection strength
β	Varied	Connection strength between cortices
n''_j	See Fig. 10a	Number of connections between cortices from the j th neuron
G''_{jk}	See Fig. 10b	Inter-cortical connection strength

TABLE I. The list of parameters used in modeling the Hindmarsh-Rose network.

It is worth noting that one of the limitations of this model is the changing nature of α and β in the actual brain. The strengths of connections and the amounts by which they are amplified vary in time. However, they will be treated as constant, in order to present a view of parameter space.

B. Network

The model was implemented on a mesoscale mouse connectome, which organized the mouse brain into 213 fine areas, grouped into 13 coarse areas, and measured the connection strengths between the subcortices³⁵. These coarse areas were used as the sets C (Eqs. (5) and (6)) for chimera and metastability analyses. The connection strengths were then reduced to those with sufficient certainty ($p < 0.01$), and segmented as follows:

$$G_{jk} = \begin{cases} 0, & \text{if } O_{jk} < 10^{-4} \\ 1, & \text{if } 10^{-4} \leq O_{jk} < 10^{-2} \\ 2, & \text{if } 10^{-2} \leq O_{jk} < 1 \\ 3, & \text{if } 1 \leq O_{jk} \end{cases} \quad (27)$$

where O_{jk} is the raw connection strength provided by³⁵. This was done to more closely match the analysis of Santos *et al.*¹².

G is shown in Fig. 9, and is shown broken down into its inter- and intra-connections in Fig. 10. A useful aspect of this brain network is that the standard graph whose topology it most resembles is a small-world or Watts-Strogatz graph³⁵. This graph topology lends itself well to the development of chimera states, as it facilitates nonlocal coupling⁸.

Another benefit to this network is that it is accurate and complete. Given the complexity of brains, creat-

ing an accurate structural or functional connectome is extremely difficult. It has yet to be done to a large-scale extent in humans, and was only recently done in mice. Additionally, as mice are common analogues for humans in laboratory settings, the mouse seemed a fitting “guinea pig” for the creation of chimera states.

C. Implementation

The modified Hindmarsh-Rose model was coded into Python (Python version 3.7.0, NumPy version 1.15.2, Pandas version 0.23.4, SciPy version 1.1.0), and integrated using a 4th-order Runge-Kutta with variable step size⁸ $dt < 0.01$. The code was verified by reproducing the results of¹². The model was run for a time period of $T_{\text{sim}} = [-1000, 5000]$, where only times $T = [0, 4000]$ were saved. The times $[-1000, 0]$ were calculated and thrown away to eliminate transients. The chimeras were extremely unlikely to be eliminated on such a time scale, due to the size of the network³⁴. The times $[4000, 5000]$ were calculated to facilitate analysis of the phase.

The phase of the j th neuron in the resulting waveform was found as

$$\phi_j(t) = 2\pi \times \frac{t - t_i}{t_{i+1} - t_i} \quad (28)$$

where t_i is the time at which the j th neuron fires (x_j crosses 0 in a positive direction) for the i th time⁹. In order for this calculation to be possible for all values in T , it was necessary to have each neuron fire at least once after T had finished (i.e., there has to be some $t_{i+1} \notin T$ in order to calculate the phase for times $t_i \leq t \leq t_{\max} = 4000$). The calculated time range went so far beyond t_{\max} so that any extremely slow-firing neurons were allowed to do so, to ensure that as much of parameter space was in the physical region (Section IV B). The phase was then used to find the chimera and metastability indices of the result using Eq. (5) and Eq. (6) respectively.

This process was repeated for various parameter sweeps of $\alpha \times \beta$, summarized in Table II. Note that the step in each strength $i \in \{\alpha, \beta\}$ is $\Delta i = \frac{i_{\max}}{n_i - 1}$, due to the fact that the ranges are inclusive of both endpoints.

⁸ Step size was determined by SciPy’s internal algorithms, but was limited to a maximum of 0.01.

⁹ This is a similar measure for the phase as was used in¹², but allows for easier discrimination between physical and aphysical parameter sets. It is modified to keep $\phi_j \in (0, 2\pi)$ and to eliminate ambiguity about the meanings of the subscripts.

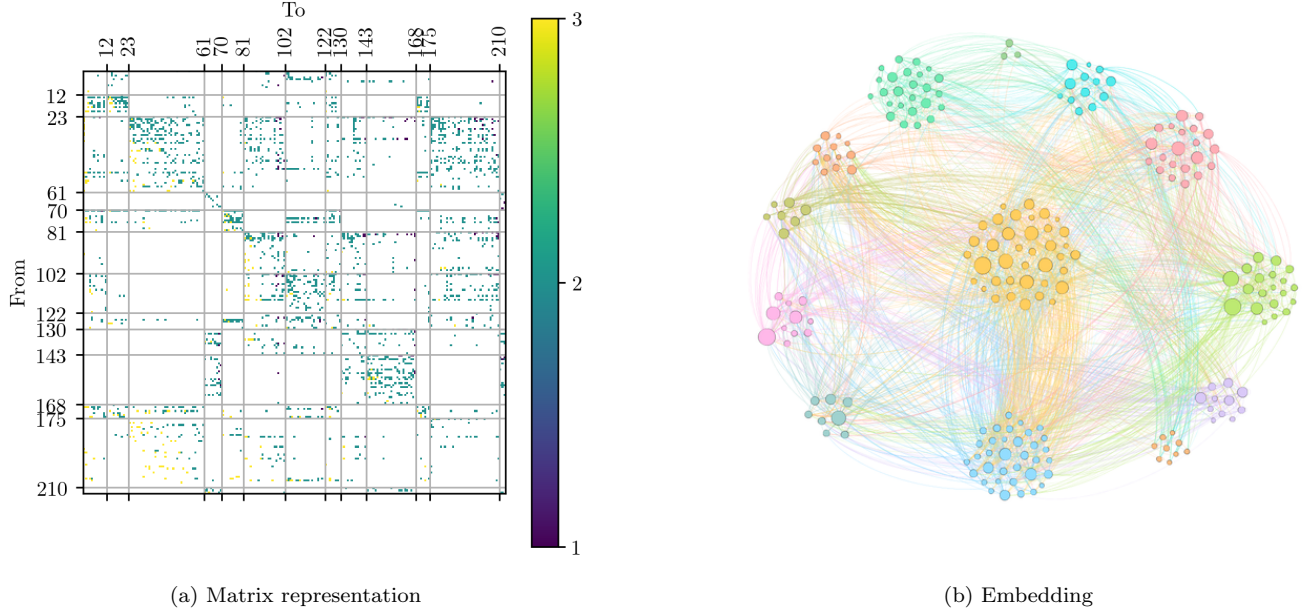


FIG. 9. (a) A matrix representation of the mouse connectome, with strengths as defined by Eq. (27). The cortices represented are, left to right (top to bottom), the striatum, the olfactory areas, the isocortex, the cerebellar cortex, the hippocampal formation, the midbrain, the hypothalamus, the pallidum, the pons, the medulla, the cortical subplate, the thalamus, and the cerebellar nuclei. (b) An embedding of the graph. Edge colors indicate the source location.

$\alpha_{\max}, \beta_{\max}$	$\Delta\alpha (n_\alpha), \Delta\beta (n_\beta)$	Figure
1.6, 0.4	0.0203 (80), 0.0211 (20)	—
3.2, 0.8	0.0405 (80), 0.0205 (40)	—
0.2, 0.1	0.00253 (80), 0.00256 (40)	Fig. 15a
0.9, 0.9	0.0101 (80), 0.0101 (80)	—
1.0, 1.0	0.0101 (100), 0.0101 (100)	Fig. 14

TABLE II. The sweeps used in evaluating the effects of α and β on the chimera and metastability indices. All parameter sweeps started at $(\alpha, \beta) = (0, 0)$. The $[0, 1] \times [0, 1]$ sweep was performed 10 times, and the resulting chimera-like indices were averaged.

Initial conditions were drawn from uniform distributions of $x_j \in [-2, 2]$, $y_j \in [0, 0.2]$, $z_j \in [0, 0.2]$. All code was run on the Vermont Advanced Computing Core, and is available online¹⁰.

IV. RESULTS

We now investigate three aspects of the results of this work. First, we compare the output from the model to real-world data, on a qualitative level. We then discuss the region of parameter space for which the model produces unphysical results. Finally, we draw connections between chimera states in the model and their physiological analogues.

A. Model Quality

It is worthwhile to first discuss the quality of the model used, and its relationship to reality. Fig. 12 shows several types of behavior one can expect on an EEG trace. Healthy brain behavior presents as low-amplitude oscillations on an EEG, as the asynchrony leads the firings of individual neurons to cancel each other out. Seizures and seizure-like activity present as higher-amplitude oscillations, as the synchrony decreases the variance between neurons, making the mean closer to the behavior of each neuron. One of the main challenges of simulating seizures is that only trained experts can truly identify seizures; as yet, there is no mathematical technique for identifying seizures²⁰.

The highly chimeric portion of the landscape appears to be mostly below the $\beta = \alpha$ line.

However, one can indicate whether a model resembles epileptiform activity on a qualitative level. Fig. 13a shows the results of a simulation of the Hindmarsh-Rose network for $(\alpha, \beta) = (0.604, 0.273)$. Qualitatively, in our simulation, the thalamus, the pons, and the striatum look like the wild type EEG; the cerebellar cortex shows some spiking behavior, as well as some spike runs; the medulla and the hypothalamus look to be in repetitive spike runs; and the cortical subplate seems to be exhibiting seizure-like behavior over some time periods. This shows that the behavior visible on an EEG can be reproduced in this model.

While getting a higher neuronal resolution from the EEG is not possible due to the nature of the method, one

¹⁰ <https://gitlab.uvm.edu/Henry.Mitchell/chimera-2019>

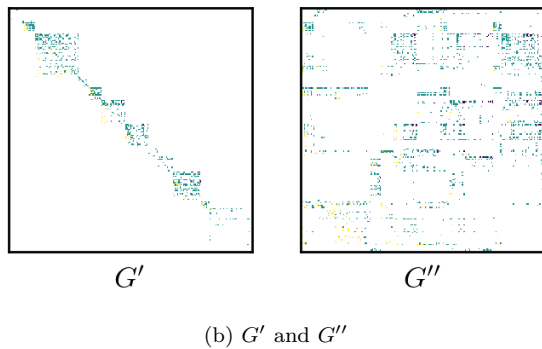
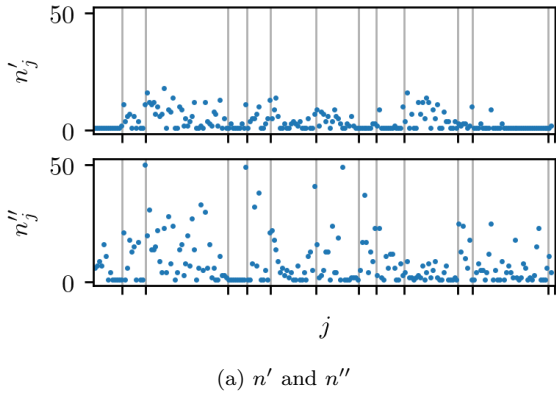


FIG. 10. A breakdown of the network. (a) shows n'_j and n''_j , effectively the number of nonzero elements in the j th row of G' and G'' , respectively. (b) shows G' and G'' , which are G (Fig. 9a) only within and between cortices, respectively.

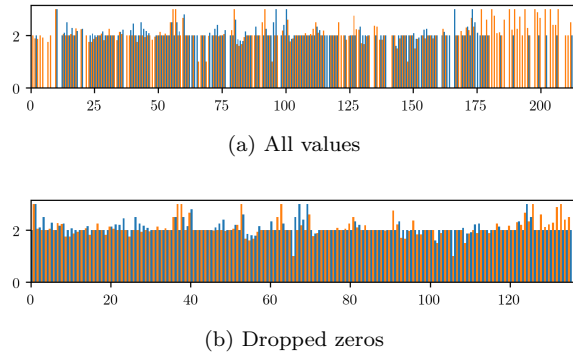


FIG. 11. The average connection strengths for each neuron j , within cortices (blue) and between them (orange). (a) All of the subcortices. (b) All of the subcortices for which neither intra- nor inter-cortical average strength was 0.

can see the neural dynamics of the model (Fig. 13b). It is evident that the thalamus, the pons, and the striatum are each highly asynchronous, which corresponds to their wild-type presentation.

Both presentation methods have their benefits, as Fig. 13a looks similar to an EEG (and therefore lends itself well to the comparison), where Fig. 13b allows us to view the individual subcortical behaviors leading to the net dynamics.

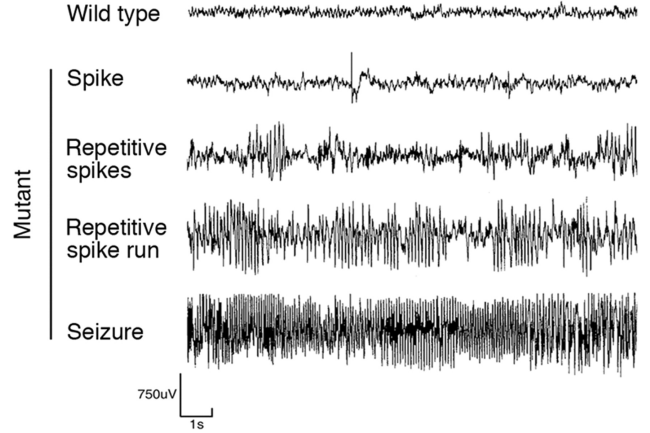


FIG. 12. A typical EEG trace. The first row (“Wild type”) shows a normal awake adult mouse EEG trace. The other four rows (“Mutant”) show typical abnormal/epileptiform activity. Taken from³⁶.

B. Aphysical Region

We choose not to include figures for the first two sweeps of Table II because a large portion of parameter space leads to an aphysical model. Specifically, for certain value pairs of (α, β) , certain neurons never fired (increased past 1). Despite the drastically increased time of evaluation (see Section III C), a vast swath of parameter space gave nonsense results (the white shown in Fig. 14). The boundary between physical and aphysical appears to be linear, with a negative slope. This means that α can range further when β is low, and vice versa. This makes sense, as increased α and β influence the model in the same way (increasing the coupling and decreasing \dot{x}_j).

Additionally, the slope of the boundary is greater than -1 , which means that α has a greater influence on the physicality of the model. This is also reasonable, but for slightly less self-evident reasons. To explain why, we must look specifically at the two coupling terms from Eq. (23):

$$-\frac{\alpha}{n'_j} \sum_{k=1}^N G'_{jk} \Theta_j(x_k) - \frac{\beta}{n''_j} \sum_{k=1}^N G''_{jk} \Theta_j(x_k)$$

This coupling will, in fact, be positive, as $\Theta_j(x_k) < 0$ if $x_j < 2$, which is true almost all of the time. This means that, as α and β increase, so does the overall coupling strength. So, there is some threshold K for which the overall coupling is too strong if

$$\frac{\alpha}{n'_j} \sum_{k=1}^N G'_{jk} |\Theta_j(x_k)| + \frac{\beta}{n''_j} \sum_{k=1}^N G''_{jk} |\Theta_j(x_k)| > K_j \quad (29)$$

for some j . So, in order for α to influence the coupling’s proximity to K more than β does, there must exist some j such that $\frac{1}{n'_j} \sum G'_{jk} |\Theta_j(x_k)| > \frac{1}{n''_j} \sum G''_{jk} |\Theta_j(x_k)|$. See-

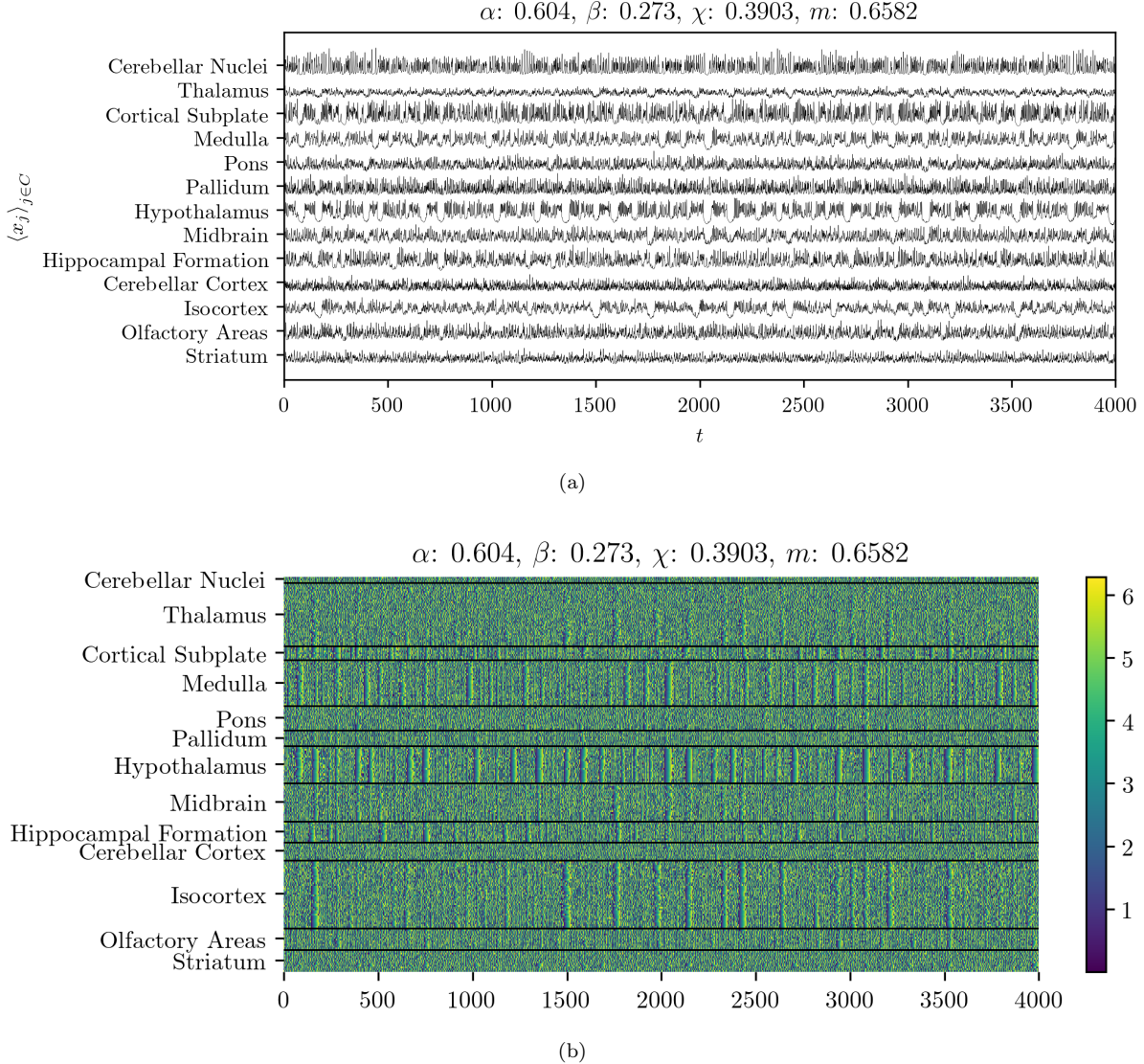


FIG. 13. A typical run of the Hindmarsh-Rose simulation. (a) The mean membrane potential within each cortex. (b) The phase ϕ of the entire timeseries for a simulation of the Hindmarsh-Rose network.

ing as $\bar{g}'_j = \frac{1}{n'_j} \sum G'_{jk}$ and $\bar{g}''_j = \frac{1}{n''_j} \sum G''_{jk}$ are the average connection strength within and between cortices (shown in Fig. 11a), these are simply a function of the topology of the graph.

It may look from Fig. 11a like β should have more influence than α , as for most j , $\bar{g}''_j > \bar{g}'_j$. However, for most of those cases, $\bar{g}''_{j_0} > \bar{g}''_{j_0} = 0$. This means that, for those j_0 , $\frac{\partial K_{j_0}}{\partial \alpha} = 0$. So, those cases contribute to the value of the threshold, but do not influence the physicality's dependence on α and β .

If we remove the j for which $\bar{g}'_j = 0$ or \bar{g}''_j , we find that, on average, $\bar{g}'_j = 2.100$, slightly more than $\bar{g}''_j = 2.079$ (see Fig. 11b). This explains the slope of the boundary between the physical region and the aphysical region.

C. Chimera states

The normalized chimera-like index of the entire physical region is shown in Fig. 14. Near the maximal edge of the physical region, the highest values of the chimera index appear to follow a slope of -1 . It is unsurprising that chimera states would be prevalent when the coupling is large (out near the boundary of the aphysical range).

What is surprising, however, is the presence of the chimeric patch in the bottom left corner of Fig. 14, shown at a higher resolution in Fig. 15a. Plotting the results of the simulations (Figs. 16a and 16b), it is evident that this is not a calculation error, but is an actual feature of the parameter landscape.

The highly chimeric portion of the landscape appears to be mostly below the $\beta = \alpha$ line. This is reasonable, as chimera states occur when coupling within groups is

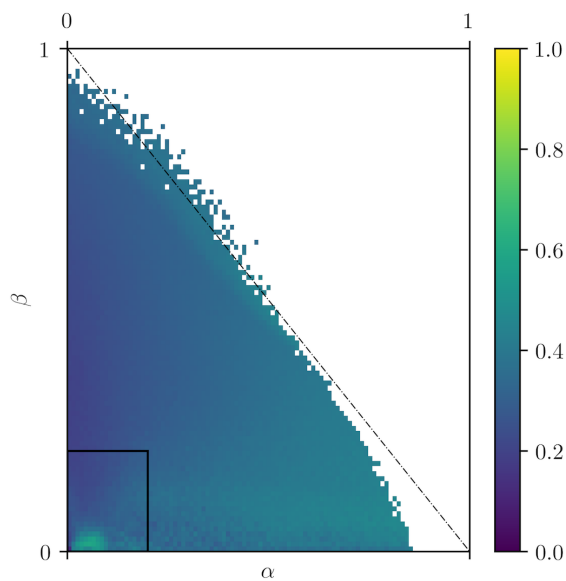


FIG. 14. The chimera-like landscape of parameter space on $(\alpha, \beta) \in (0, 1.0) \times (0, 1.0)$. The unphysical region of the model is shown in white. The black rectangle in the bottom left corner indicates the region of parameter space shown in Fig. 15a. The dashed line has a slope of -1 , to serve as a guide for Section IV C. The chimera-like index (defined in Eq. (5)) is normalized to $\frac{1}{7}$, as usual.

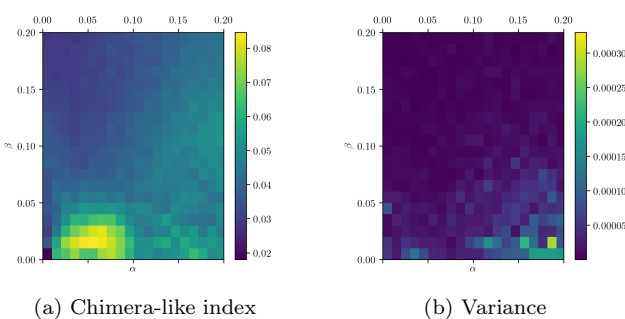


FIG. 15. The chimera index of runs with $(\alpha, \beta) \in (0, 0.2) \times (0, 0.2)$. As before, the chimera-like index is normalized to $\frac{1}{7}$. Note that the values of the index are much higher in this patch than in most of the rest of $(\alpha, \beta) \in (0, 1) \times (0, 1)$ (Fig. 14). The dashed line shows $\beta = \alpha$.

greater than coupling between groups. A small portion of the chimeric patch lies above the $\beta = \alpha$ line, likely due to the fact that the average strength between cortices is greater than the average strength within cortices (see Fig. 11a).

χ greatly lessens at $\alpha \approx 0.1$. A possible explanation for this comes from comparing the order of \dot{x} without the coupling terms, and the coupling terms themselves. From our simulation, we find that \dot{x} without the coupling terms ranges roughly from -6 to 3. The coupling terms

each¹¹ range from 0 to approximately 30α . That means that, when $\alpha > 0.1$, the coupling is at least of the same order as the sum of the rest of the terms in the equation. This leads to a qualitative difference between the two states, which likely manifests itself as the less chimeric states.

V. DISCUSSION

The logical next step is to compare the simulated EEG traces to actual data collected from mice, with the aid of an epileptologist. With that further work, this research could potentially go from a mathematical curiosity to an applicable therapeutic and diagnostic tool.

Additionally, finding an instructive phase-space embedding of the Hindmarsh-Rose network would be challenging (seeing as it is a 639-dimensional system, currently), but would likely reveal potentially useful insights into the nature of the mechanisms underlying these systems. The same could be said for Lyapunov analysis, as well as finding an informative way to create a bifurcation diagram and perform more in-depth bifurcation analysis.

Another way this work could be extended is by looking at chimera state collapse and its relationship to secondary seizure generalization. However, it would be extremely computationally expensive, given the size of the system, and would therefore require some clever handiwork³⁴.

Future work will be performed on better, more up-to-date connectomes³⁷.

- ¹J. P. Ramirez, L. A. Olvera, H. Nijmeijer, and J. Alvarez, “The sympathy of two pendulum clocks: beyond huygens’ observations,” *Scientific Reports* **6** (2016), 10.1038/srep23580.
- ²J. Pantaleone, “Synchronization of metronomes,” *American Journal of Physics* **70**, 992–1000 (2002).
- ³Y. Kuramoto and D. Battogtokh, “Coexistence of coherence and incoherence in nonlocally coupled phase oscillators,” arXiv e-prints , cond-mat/0210694 (2002), arXiv:cond-mat/0210694 [cond-mat.stat-mech].

⁴D. M. Abrams and S. H. Strogatz, “Chimera states for coupled oscillators,” *Physical Review Letters* **93** (2004), 10.1103/physrevlett.93.174102.

⁵D. M. Abrams, R. Mirollo, S. H. Strogatz, and D. A. Wiley, “Solvable model for chimera states of coupled oscillators,” *Physical Review Letters* **101** (2008), 10.1103/physrevlett.101.084103.

⁶E. A. Martens, S. Thutupalli, A. Fourrière, and O. Hallatschek, “Chimera states in mechanical oscillator networks,” *Proceedings of the National Academy of Sciences* **110**, 10563–10567 (2013).

⁷M. Shanahan, “Metastable chimera states in community-structured oscillator networks,” *Chaos: An Interdisciplinary Journal of Nonlinear Science* **20**, 013108 (2010).

⁸J. Hizanidis, N. E. Kouvaris, G. Zamora-López, A. Díaz-Guilera, and C. G. Antonopoulos, “Chimera-like states in modular neural networks,” *Scientific Reports* **6** (2016), 10.1038/srep19845.

¹¹ Since the same can be said for both α and β , we will discuss only α , with the understanding that β could be substituted into the proceeding sentences.

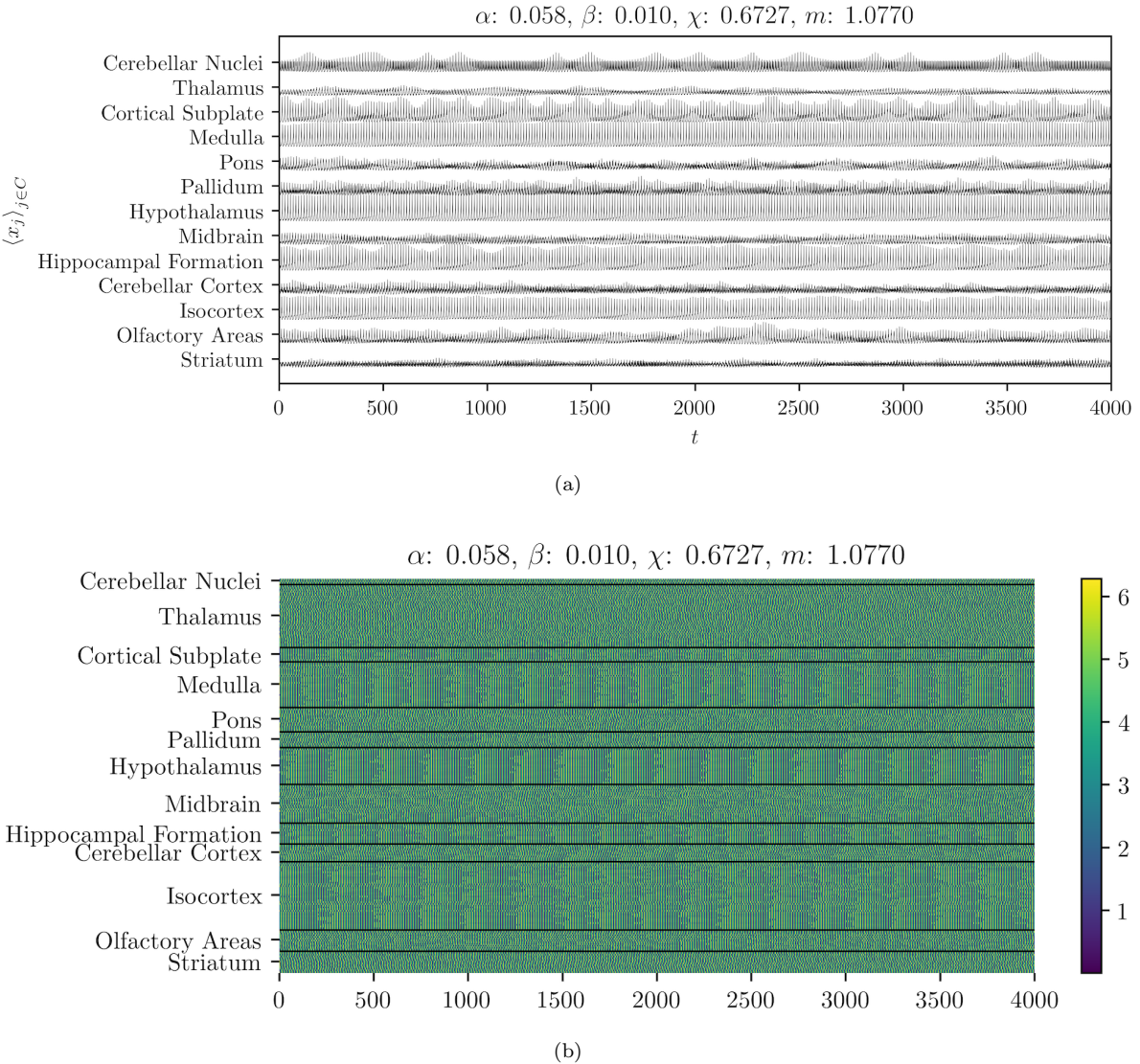


FIG. 16. A run of the Hindmarsh-Rose simulation in the chimeric island. (a) The mean membrane potential within each cortex. (b) The phase ϕ of the entire timeseries for a simulation of the Hindmarsh-Rose network. Synchronization is most consistently evident in the medulla, the hypothalamus, and the isocortex.

- ⁹R. G. Andrzejak, C. Rummel, F. Mormann, and K. Schindler, “All together now: Analogies between chimera state collapses and epileptic seizures,” *Scientific Reports* **6** (2016), 10.1038/srep23000.
- ¹⁰M. J. Panaggio and D. M. Abrams, “Chimera states: coexistence of coherence and incoherence in networks of coupled oscillators,” *Nonlinearity* **28**, R67–R87 (2015).
- ¹¹M. Santos, J. Szezech, A. Batista, I. Caldas, R. Viana, and S. Lopes, “Recurrence quantification analysis of chimera states,” *Physics Letters A* **379**, 2188–2192 (2015).
- ¹²M. Santos, J. Szezech, F. Borges, K. Iarosz, I. Caldas, A. Batista, R. Viana, and J. Kurths, “Chimera-like states in a neuronal network model of the cat brain,” *Chaos, Solitons & Fractals* **101**, 86–91 (2017).
- ¹³N. Kruk, Y. Maistrenko, and H. Koepll, “Self-propelled chimeras,” *Physical Review E* **98** (2018), 10.1103/physreve.98.032219.
- ¹⁴J. Xie, E. Knobloch, and H.-C. Kao, “Multicluster and traveling chimera states in nonlocal phase-coupled oscillators,” *Physical Review E* **90** (2014), 10.1103/physreve.90.022919.
- ¹⁵G. Deco, V. K. Jirsa, P. A. Robinson, M. Breakspear, and

- K. Friston, “The dynamic brain: From spiking neurons to neural masses and cortical fields,” *PLoS Computational Biology* **4**, e1000092 (2008).
- ¹⁶C. Molnar and J. Gair, “Concepts of biology - 1st canadian edition,” (OpenStax College, 2013) Chap. 16.1 - Neurons and Glial Cells.
- ¹⁷P. Graben, C. Zhou, M. Thiel, and J. Kurths, *Lectures in Supercomputational Neuroscience: Dynamics in Complex Brain Networks*, Understanding Complex Systems (Springer Berlin Heidelberg, 2007).
- ¹⁸M. Breakspear, “Dynamic models of large-scale brain activity,” *Nature Neuroscience* **20**, 340–352 (2017).
- ¹⁹Y. Wang, M. Goodfellow, P. N. Taylor, and G. Baier, “Phase space approach for modeling of epileptic dynamics,” *Physical Review E* **85** (2012), 10.1103/physreve.85.061918.
- ²⁰G. L. Westbrook, “Seizures and epilepsy,” in *Principles of Neural Science*, edited by E. R. Kandel, J. H. Schwartz, T. M. Jessell, S. A. Siegelbaum, and A. Hudspeth (McGraw Hill Medical, 2013) Chap. 50, pp. 1116–1139, 5th ed.
- ²¹P. N. Taylor, M. Goodfellow, Y. Wang, and G. Baier, “Towards a large-scale model of patient-specific epileptic spike-wave dis-

- charges,” *Biological Cybernetics* **107**, 83–94 (2012).
- ²²L. Leistritz, P. Putsche, K. Schwab, W. Hesse, T. Süße, J. Haueisen, and H. Witte, “Coupled oscillators for modeling and analysis of EEG/MEG oscillations,” *Biomedizinische Technik/Biomedical Engineering* **52**, 83–89 (2007).
- ²³A. Fadiman, *The Spirit Catches You and You Fall Down: A Hmong Child, Her American Doctors, and the Collision of Two Cultures*, FSG Classics (Farrar, Straus and Giroux, 1998).
- ²⁴G. Baier, M. Goodfellow, P. N. Taylor, Y. Wang, and D. J. Garry, “The importance of modeling epileptic seizure dynamics as spatio-temporal patterns,” *Frontiers in Physiology* **3** (2012), 10.3389/fphys.2012.00281.
- ²⁵V. K. Jirsa, W. C. Stacey, P. P. Quilichini, A. I. Ivanov, and C. Bernard, “On the nature of seizure dynamics,” *Brain* **137**, 2210–2230 (2014).
- ²⁶V. Jirsa, T. Proix, D. Perdikis, M. Woodman, H. Wang, J. Gonzalez-Martinez, C. Bernard, C. Bénar, M. Guye, P. Chauvel, and F. Bartolomei, “The virtual epileptic patient: Individualized whole-brain models of epilepsy spread,” *NeuroImage* **145**, 377–388 (2017).
- ²⁷S. H. Strogatz, *Nonlinear Dynamics and Chaos: With Applications to Physics, Biology, Chemistry, and Engineering*, 1st ed. (Westview Press, 2015).
- ²⁸M. Breakspear, J. A. Roberts, J. R. Terry, S. Rodrigues, N. Mahant, and P. A. Robinson, “A unifying explanation of primary generalized seizures through nonlinear brain modeling and bifurcation analysis,” *Cerebral Cortex* **16**, 1296–1313 (2005).
- ²⁹F. Marten, S. Rodrigues, O. Benjamin, M. P. Richardson, and J. R. Terry, “Onset of polyspike complexes in a mean-field model of human electroencephalography and its application to absence epilepsy,” *Philosophical Transactions of the Royal Society A: Mathematical, Physical and Engineering Sciences* **367**, 1145–1161 (2009).
- ³⁰K. Höhlein, F. P. Kemeth, and K. Krischer, “Lyapunov Analysis of Chimera States in Globally Coupled Stuart-Landau oscillators,” arXiv e-prints , arXiv:1905.00218 (2019), arXiv:1905.00218 [nlin.CD].
- ³¹K. Bansal, J. O. Garcia, S. H. Tompson, T. Verstynen, J. M. Vettel, and S. F. Muldoon, “Cognitive chimera states in human brain networks,” *Science Advances* **5**, eaau8535 (2019).
- ³²T. Chouzouris, I. Omelchenko, A. Zakharova, J. Hlinka, P. Jiruska, and E. Schöll, “Chimera states in brain networks: Empirical neural vs. modular fractal connectivity,” *Chaos: An Interdisciplinary Journal of Nonlinear Science* **28**, 045112 (2018).
- ³³A. Schmidt, T. Kasimatis, J. Hizanidis, A. Provata, and P. Hövel, “Chimera patterns in two-dimensional networks of coupled neurons,” *Physical Review E* **95** (2017), 10.1103/physreve.95.032224.
- ³⁴M. Wolfrum and O. E. Omel’chenko, “Chimera states are chaotic transients,” *Physical Review E* **84** (2011), 10.1103/physreve.84.015201.
- ³⁵S. W. Oh, J. A. Harris, L. Ng, B. Winslow, N. Cain, S. Mihalas, Q. Wang, C. Lau, L. Kuan, A. M. Henry, M. T. Mortrud, B. Ouellette, T. N. Nguyen, S. A. Sorensen, C. R. Slaughterbeck, W. Wakeman, Y. Li, D. Feng, A. Ho, E. Nicholas, K. E. Hirokawa, P. Bohn, K. M. Joines, H. Peng, M. J. Hawrylycz, J. W. Phillips, J. G. Hohmann, P. Wohnoutka, C. R. Gerfen, C. Koch, A. Bernard, C. Dang, A. R. Jones, and H. Zeng, “A mesoscale connectome of the mouse brain,” *Nature* **508**, 207–214 (2014).
- ³⁶M. C. Ljungberg, C. N. Sunnen, J. N. Lugo, A. E. Anderson, and G. D’Arcangelo, “Rapamycin suppresses seizures and neuronal hypertrophy in a mouse model of cortical dysplasia,” *Disease Models & Mechanisms* **2**, 389–398 (2009).
- ³⁷J. E. Knox, K. D. Harris, N. Graddis, J. D. Whitesell, H. Zeng, J. A. Harris, E. Shea-Brown, and S. Mihalas, “High-resolution data-driven model of the mouse connectome,” *Network Neuroscience* **3**, 217–236 (2019).

Appendix A: Acknowledgments

This work could not have been completed without help from Taras Lakoba and Sean Flynn. The authors also thank Kameron Harris for helpful comments on the manuscript.

Appendix B: Additional Figures

Fig. 17 shows some additional analyses of the parameter landscape.

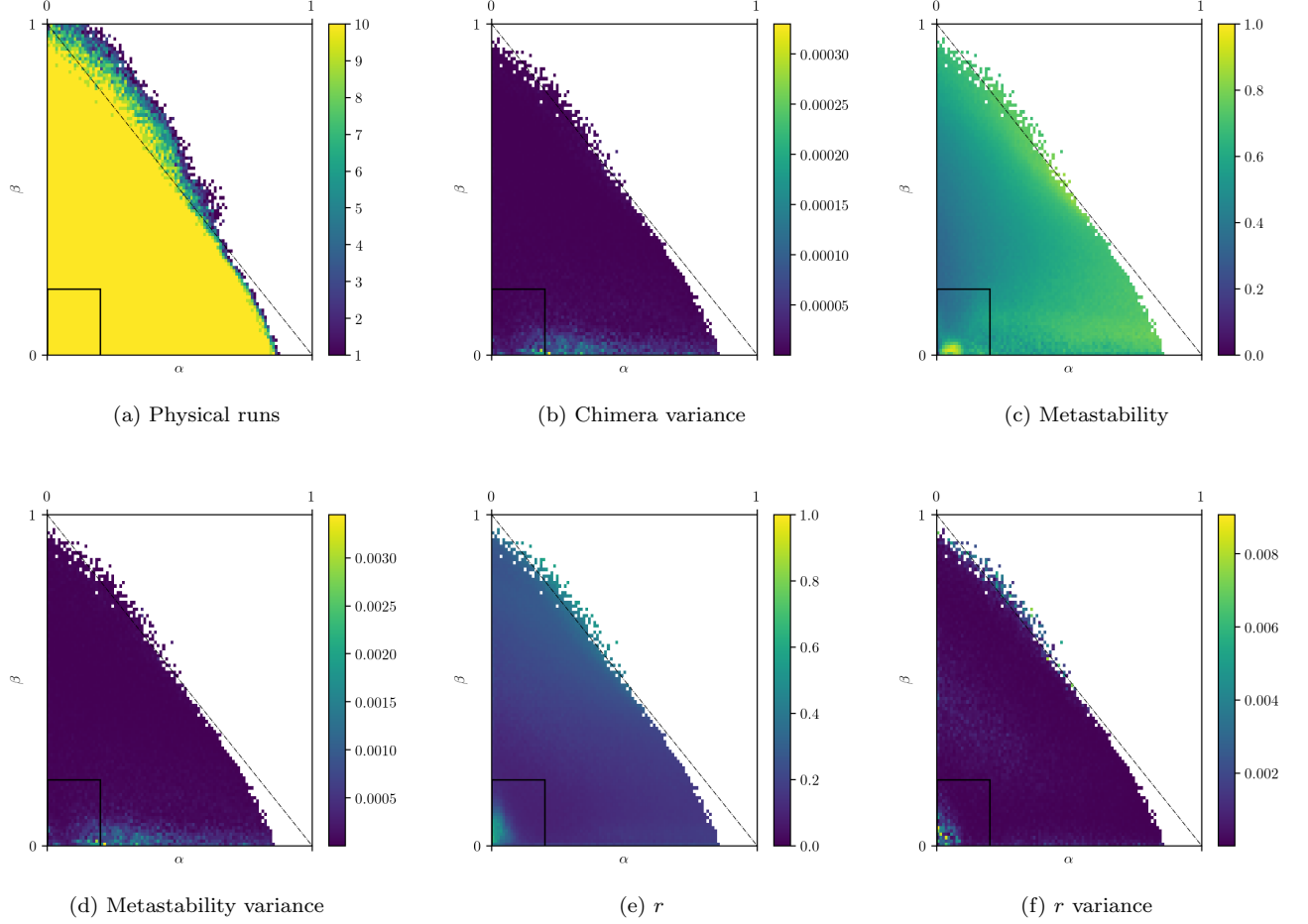


FIG. 17. Additional analyses of the parameter landscape. Fig. 17a shows the number of runs (out of 10) which gave physical results. All parameter sets which are not yellow in Fig. 17a were excluded from the other analyses. Fig. 17b shows the variance of the chimera-like index. Fig. 17c shows the metastability index. Fig. 17d shows the variance of the metastability index. Fig. 17e shows the mean order parameter over time, averaged across runs. Fig. 17f shows the variance between runs of the mean order parameter.